Huang, M.-H., Fielding, E. J., Liang, C., Milillo, P., Bekaert, D., Dreger, D., Salzer, J. T. (2017): Coseismic deformation and triggered landslides of the 2016 Mw 6.2 Amatrice earthquake in Italy. - *Geophysical Research Letters*, *44*, 3, pp. 1266—1274.

DOI: http://doi.org/10.1002/2016GL071687

AGU PUBLICATIONS

Geophysical Research Letters

RESEARCH LETTER
10.1002/2016GL071687

Key Points:
- InSAR can provide coseismic displacement or other hazard response typically within a few days
- Nearly all of the slip occurred between 3 and 5 km in depth but extends about 20 km along strike
- The triggered landslide on the Monte Vettore fault may contribute additional fault offset and influence the long-term fault slip rate

Supporting Information:
- Supporting Information S1

Correspondence to:
M.-H. Huang,
Mong-Han.Huang@jpl.nasa.gov

Citation:
Huang, M.-H., E. J. Fielding, C. Liang, P. Milillo, D. Bekaert, D. Dreger, and J. Salzer (2017), Coseismic deformation and triggered landslides of the 2016 M_w 6.2 Amatrice earthquake in Italy, *Geophys. Res. Lett.*, *44*, 1266–1274, doi:10.1002/2016GL071687.

Received 25 OCT 2016
Accepted 18 JAN 2017
Accepted article online 20 JAN 2017
Published online 4 FEB 2017

Coseismic deformation and triggered landslides of the 2016 M_w 6.2 Amatrice earthquake in Italy

Mong-Han Huang[1], Eric J. Fielding[1], Cunren Liang[1], Pietro Milillo[1], David Bekaert[1], Douglas Dreger[2], and Jacqueline Salzer[3]

[1]Jet Propulsion Laboratory, California Institute of Technology, Pasadena, California, USA, [2]Berkeley Seismological Laboratory, University of California, Berkeley, California, USA, [3]Physics of Earthquakes and Volcanoes, GFZ German Research Centre for Geosciences, Potsdam, Germany

Abstract The Central Apennines in Italy have had multiple moderate-size but damaging shallow earthquakes. In this study, we optimize the fault geometry and invert for fault slip based on coseismic GPS and interferometric synthetic aperture radar (InSAR) for the 2016 M_w 6.2 Amatrice earthquake in Italy. Our results show that nearly all the fault slip occurred between 3 and 6 km depth but extends 20 km along strike. There was less than 4 cm static surface displacement at the town Amatrice where the most devastating damage occurred. Landslides triggered by earthquake ground shaking are not uncommon, but triggered landslides with submeter movement are challenging to be observed in the field. We find evidence of coseismically triggered deep-seated landslides northwest and northeast of the epicenter where coseismic peak ground acceleration was estimated >0.5 g. By combining ascending and descending InSAR data, we are able to estimate the landslide thickness as at least 100 and 80 m near Monte Vettore and west of Castelluccio, respectively. The landslide near Monte Vettore terminates on the preexisting fault Monte Vettore Fault (MVEF) scarp. Our results imply that the long-term fault slip rate of MVEF estimated based on paleoseismic studies could potentially have errors due to triggered landslides from nearby earthquake events.

1. Introduction

Seven years after the 2009 M_w 6.3 L'Aquila earthquake in Italy, the devastating Amatrice earthquake struck the region on 24 August 2016, ~40 km NW of L'Aquila, producing severe damage in several towns in the Apennines including Amatrice and Norcia (Figure 1). The W-phase moment tensor resolved by the U.S. Geological Survey National Earthquake Information Center (NEIC) suggests a M_w 6.2 normal fault event at ~11 km depth [*National Earthquake Information Center* (*NEIC*), 2016]. Both the NEIC and the Global Centroid Moment Tensor (GCMT) [*Dziewonski* et al., 1981; http://www.globalcmt.org/] solutions show a similar strike, dip, and rake of the focal mechanism (165°/49°/−78° from NEIC and 145°/38°/−101° from GCMT). The 2016 Amatrice earthquake largely fills a gap between the September 1997 Colfiorito earthquake sequence in Umbria-Marche [*Margheriti et al.*, 1998; *Stramondo et al.*, 1999; *Lundgren and Stramondo*, 2002] to the north and the 2009 L'Aquila earthquake to the south [*Atzori et al.*, 2009; *Cheloni et al.*, 2014]. This region is part of the Central Apennine Mountains within faulted blocks bounded by normal faults, mostly trending NW-SE, NNW-SSE, and NE-SW [*Blumetti et al.*, 1993; *Boncio et al.*, 2004]. Active extensional tectonics of about 3 mm/yr plays a major role in the slope morphogenesis of the area [*D'Agostino et al.*, 2008; *Galli et al.*, 2009; *D'Agostino*, 2014].

Despite the lack of historic earthquake records in the Italian parametric earthquake catalogue (CPTI15) for mountainous and sparely populated regions in the Central Apennines, the earliest reported earthquake (M_w 5.3) was found to date back to 1627 [*Rovida et al.*, 2016]. The strongest historical event was reported in 1639, characterized by a series of five seismic events localized close to Amatrice [*Postpischl*, 1985; *Monachesi and Castelli*, 1992]. The 1639 earthquake was followed by two events in the next 35 years with magnitudes less than 6 (e.g., M_w 5.9 in Monti della Laga and M_w 5.3 in Amatrice). A few more events have been recorded in Accumoli (M_w 5.1 in 1883, M_w 4.6 in 1910, and M_w 4.7 in 1950) and in Amatrice (M_w 4.7 in 1963). Ever since the start of the instrumental records, the Italian Servizio Sismico Nazionale network has recorded several minor earthquakes ($M \leq 4$) in this region [*Boncio et al.*, 2004]. North of the 2016 Amatrice earthquake epicenter, the Monte Vettore Fault (MVEF) was identified from geomorphology and paleoseismology. Based on trench work, *Galadini and Galli* [2003] estimated 0.11–0.36 mm/yr long-term fault slip

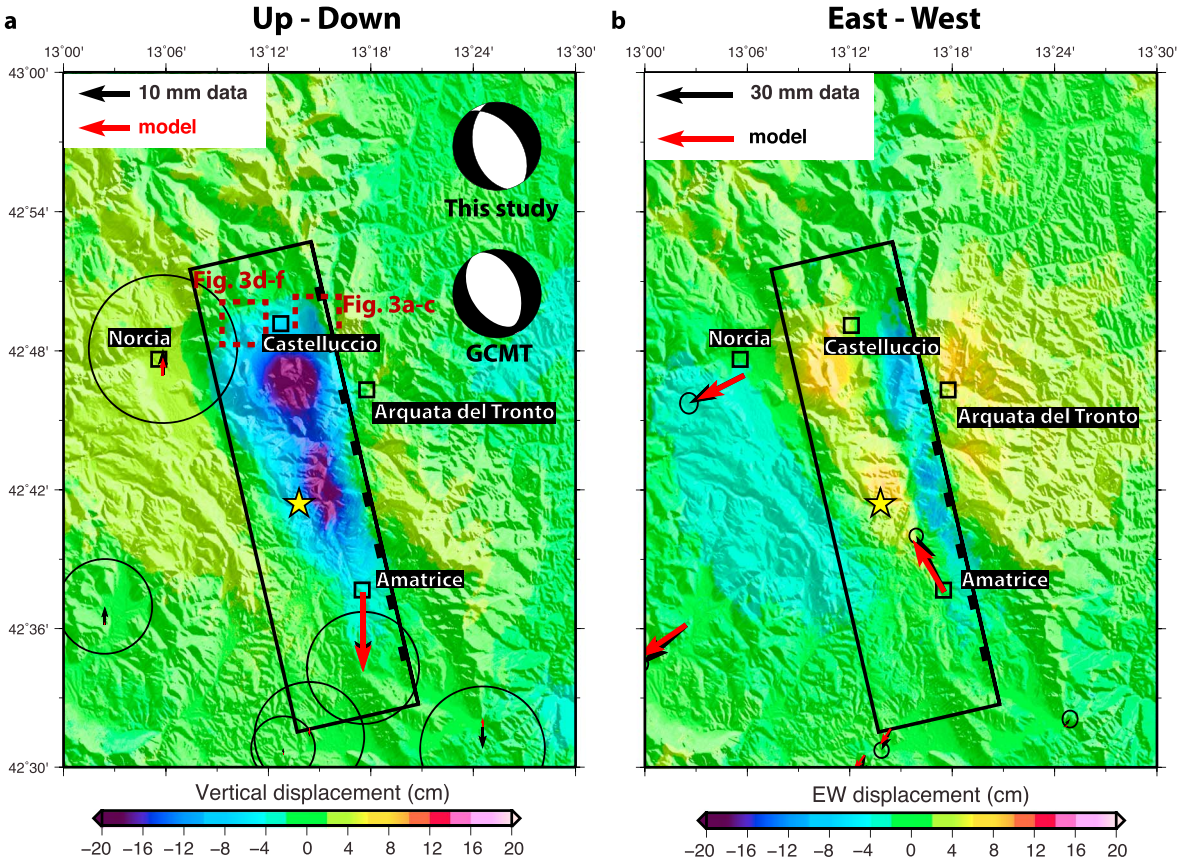

Figure 1. Coseismic displacement in (a) vertical and (b) horizontal components based on decomposing Sentinel-1 ascending and descending interferograms. The yellow star shows the epicenter based on *Piccardi et al.* [2016]. The black rectangle shows the outline of the fault plane inferred in this study. The focal mechanisms show different moment tensor solutions from GCMT and this study. Note less than 4 cm static coseismic displacement in Amatrice.

rate along the MVEF with earthquake recurrence interval no longer than 4690 years. They also suggested that the MVEF is capable of *M* 6.5 events.

Preliminary field investigations conducted by the Italian Istituto Nazionale di Geofisica e Vulcanologia (*INGV*) reveal severe building damage in Amatrice, Arquata del Tronto, and Norcia [*INGV Working Group*, 2016; *Cimellaro*, 2016; *Piccardi et al.*, 2016; *Gruppo di Lavoro INGV sul Terremoto di Amatrice*, 2016] (see Figure 1 for locations). Additionally, an ~5 km long surface rupture with up to 30 cm peak offset was found SW of Monte Vettore and southward [*Piccardi et al.*, 2016]. However, whether these surface ruptures are associated with shallow fault slip along MVEF or landslides triggered by coseismic ground motion cannot be easily discriminated from field investigation alone.

In this study, we combine interferometric synthetic aperture radar (InSAR) (Sentinel-1A/Sentinel-1B and ALOS-2) and GPS measurements to constrain the fault geometry and slip distribution of the Amatrice earthquake. We calculate coseismic Coulomb stress change to understand the connection between stress change and aftershock locations and localized deformations. In addition, we use high spatial resolution (~5 m) Cosmo-SkyMed (CSK) SAR data in combination with a TanDEM-X digital elevation model (DEM) to investigate the localized surface deformation found in Monte Vettore foothills and west of Castelluccio. We demonstrate how geodetic data can reveal a quick response to earthquake and other natural hazards, which is critical for identifying type of damage as well as imaging earthquake source slip distribution.

2. Data

We use four SAR acquisitions from Sentinel-1A/Sentinel-1B, operated under the Copernicus program by the European Space Agency, four from ALOS-2 satellites operated by Japan Aerospace Exploration Agency

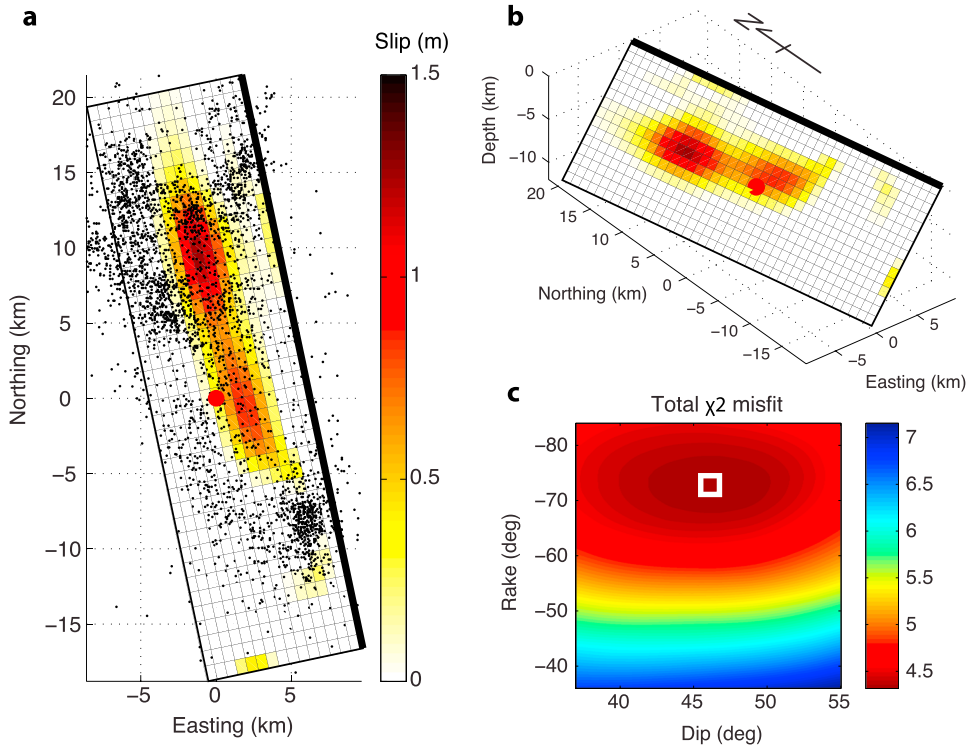

Figure 2. Fault slip distribution. (a) Map view of slip distribution based on the best fitting model. The color of each fault patch represents the amount of fault slip. The black dots show 1 week long aftershocks from the ISIDE INGV database. The thick black line indicates the projection of the fault at the surface. The red dot indicates the earthquake hypocenter based on *Piccardi et al.* [2016]. (b) A 3-D view of the fault slip distribution from the southwest. (c) Grid search χ^2 error estimates of model fits for ranges of fault dip and rake. The white square indicates the fault dip and rake for the optimal fault model.

(JAXA), and two from COSMO-SkyMed (CSK) operated by the Italian Space Agency (ASI) to generate two ascending and three descending coseismic interferograms (Table S1 in the supporting information). The wavelengths of Sentinel-1A/Sentinel-1B, ALOS-2, and CSK sensors are 5.6 cm, 24.2 cm, and 3.12 cm, respectively. The Sentinel-1 data are acquired in Terrain Observation by Progressive Scans (TOPS) mode and processed up to interferograms using the TopsApp module of the InSAR Scientific Computing Environment (ISCE) software [*Rosen et al.*, 2012]. The ALOS-2 scenes were acquired in stripmap mode (two frames per acquisition) and processed using ISCE as well. Note that the postearthquake ascending ALOS-2 scene was acquired by JAXA less than 24 h after the earthquake (Table S1). We process each ALOS-2 frame up to the single look interferogram stage, after which interferograms are mosaicked, and the remaining steps are performed on the mosaicked interferogram. The processing of the CSK data set is similar to that processed for the ALOS-2 data set using ISCE extensions. We processed the CSK interferogram with a small number of looks to maintain as much of the fine detail in the fringes as possible, resulting in a final interferogram spacing of 5 m. Here we only present one frame from a descending track (Table S1) with an incidence angle of ~36°. The high spatial resolution and high signal-to-noise ratio of CSK InSAR phase enable mapping fine details of the surface deformation. We use the 1 arc sec (~30 m) Shuttle Radar Topography Mission version 3 digital elevation model [*Farr et al.*, 2007] to correct the phase due to topography and unwrap the interferograms using *Snaphu* 1.4.2 [*Chen and Zebker*, 2002]. To reduce computational effort of our finite source modeling, we subsample each interferogram on uniform grids to approximately four observations per square kilometer. We preserve the observations in the area between longitude 13°E–13.5°E and latitude 42.4°N–43°N, leading to a total of 8906 observations for Sentinel-1A/Sentinel-1B and 8796 for ALOS-2.

We use the coseismic GPS measurements provided by *INGV* [2016] (Figure S2). There are 106 stations with three-component coseismic offset estimates available online (http://ring.gm.ingv.it/wp-content/uploads/2016/08/CombinedGPS_Offsets_v4R.dat). We do not include station GUB2 due to abnormal high vertical

displacement in the far field. The coseismic measurements were estimated based on 3 days of continuous GPS stations position before and after the main shock, and the stations are generally within 100 km from the epicenter [*INGV*, 2016].

3. Method

We perform geodetic modeling using a layered elastic Earth structure, where the Green's functions are computed using the *EDGRN/EDCMP* programs [*Wang et al*., 2003] and the velocity structure based on *Cirella et al*. [2012]. We calculate the Green's functions with 1 km interval vertically between 0 and 15 km depth and 1 km interval laterally within a 500 km radius from the epicenter. We construct a 39 km × 15 km fault plane with 1 km × 1 km subfault patch size. For each subfault, we choose the closest Green's function in distance from a subfault slip to a given surface observation. We assume uniform rake distribution, and there is no fault-opening motion. We use a nonnegative least squares subroutine to calculate slip on each subfault patch with the method developed in *Kaverina et al*. [2002], and we assign initial weighting for each GPS or InSAR datum sample based on its uncertainty. The GPS uncertainties are provided in *INGV* [2016], and the InSAR uncertainties are considered as the variance term in equation (2) introduced later. We determine the fault strike based on inspecting the orientation of the zero crossing in the line of sight displacement changes from range shortening to lengthening in both ascending and descending interferograms (Figure 1). We find the fault strike as 167°, which is 2° more clockwise from the U.S. Geological Survey (USGS) NEIC solution but strongly constrained by the InSAR data.

In our inversion, we first set the initial fault dip and rake based on the NEIC solution in order to determine the relative weighting between GPS and InSAR data sets and the Laplacian smoothing value for the inverted slip distribution [*Huang et al*., 2013]. The relative weighting is an additional weighting for all GPS measurements relative to the InSAR data sets. Once the weighting and smoothing parameters are determined, we vary the fault dip and rake angles by ±20° from the NEIC solution. The inferred fault geometry is based on the dip and rake combination with the lowest model misfit.

Here we use the χ^2 errors to describe the model misfit,

$$\chi^2 = \frac{1}{N}[\boldsymbol{d} - \boldsymbol{Gm}]^T \boldsymbol{C}^{-1}[\boldsymbol{d} - \boldsymbol{Gm}], \tag{1}$$

where $\boldsymbol{d}$ are the observations, $\boldsymbol{Gm}$ the forward prediction, and N the total number of observation (three components for GPS and one for InSAR). The covariance matrix $\boldsymbol{C}$ contains the GPS and InSAR covariance. We assume that the GPS uncertainties are not spatially correlated, so the off-diagonal terms in the GPS covariance matrix are zeros. For InSAR, we estimate each InSAR covariance matrix from individual interferogram with the coseismic region removed. Prior to the calculation of the experimental variogram, we ensure second-order stationarity of the InSAR data by removing a linear ramp from the interferogram. The experimental covariance function $\boldsymbol{C}(h)$ is defined [*Sudhaus and Jonsson*, 2009; *Bekaert et al*., 2015a]

$$C(h) = \begin{cases} \sigma_o^2 & , \text{ for } h = 0 \\ \sigma_{\text{exp}}^2 \cdot e^{-h/c} + d & , \text{ for } h > 0 \end{cases}, \tag{2}$$

where σ_o^2 and σ_{exp}^2 are the observation and experiment variance, respectively. c and d are constants to fit observed variance, and h is the separation distance between InSAR observations (Figure S3).

4. Results

The ascending and descending Sentinel-1 and ALOS-2 interferograms are shown in Figure S1, and Figure 1 shows the vertical and horizontal (mostly east-west) displacements based on the ascending and descending Sentinel-1 interferograms using equation (S7) in supporting information Text S1 [also *Fialko et al*., 2001]. InSAR results show that most of the coseismic displacement is in vertical direction. There are two main coseismic subsidence areas with peak vertical displacement ~20 cm and ~19 cm north and east of the epicenter (the star in Figure 1), respectively. To the south in Amatrice where the highest fatality and building damage were, we find ~3 cm coseismic displacement in both vertical and horizontal directions from both InSAR and GPS (Figure 1). This result implies that the damage of the town is mostly due to severe dynamic ground motion, directivity, and/or basin amplifications, as the static displacements are small.

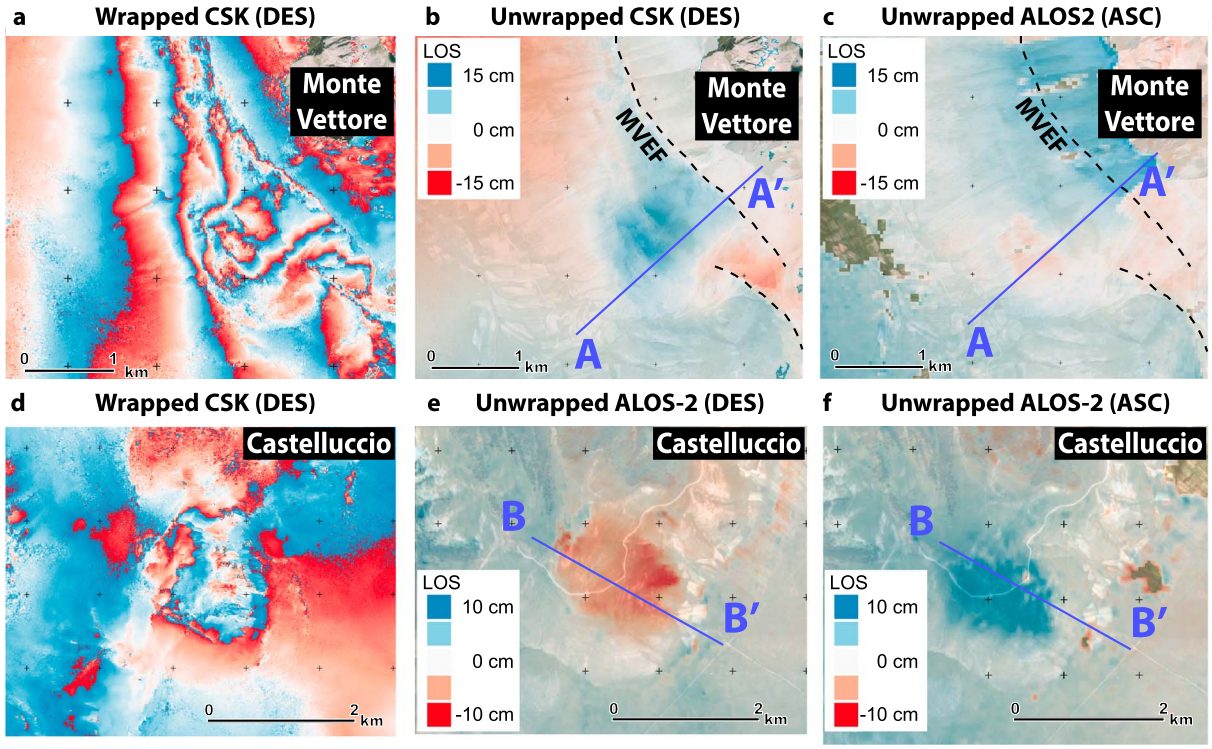

Figure 3. Triggered landslides in areas of (a–c) Monte Vettore and (d–f) west of Castelluccio. Note that the displacement associated with the main fault slip at depth has been removed based on our preferred model (Figure 2). See Figure 1 for locations of the two landslides. The interferograms (Figures 3a and 3d) shown in this figure are based on the COSMO-SkyMed satellite image pair (20–28 August 2016), and they are rewrapped to 4 cm interval. Other interferograms are from ALOS-2 pairs (Table S1). The warm and cold colors indicate range decrease and increase, respectively. In Figure 3c, the blue color north of Monte Vettore Fault (MVEF) is due to phase unwrapping error instead of real deformation. Background images from Google Maps, plotted with the open source software QGIS 2.12.

In the geodetic inversion, the GPS relative weighting and the model smoothing values are 0.5 and 0.004, respectively (Figures S4a and S4b). Figure S4c shows χ^2 of InSAR and GPS data sets, and Figure 2c shows χ^2 of combined InSAR and GPS data sets. Figure S4d shows the histograms of InSAR and GPS misfits based on the optimal fault geometry. As most of the data covariance is due to tropospheric water vapor, this likely reflects the atmospheric conditions at the different acquisition times [*Bekaert et al.*, 2015b]. For the L-band ALOS-2 data, the interferograms are also more sensitive to ionospheric perturbation that could produce longer-wavelength correlated noise such as the descending pair (Figure S3d).

Our optimized fault geometry (Figure 2) infers a 46° west dipping normal fault with rake as −73°. The inferred fault dip and rake are about the same as of the GCMT and NEIC solutions. The χ^2 errors (equation (1)) of our inferred slip distribution are 0.9 for GPS and 8.0 for InSAR, and the inferred moment is 1.88×10^{18} N m, equivalent to M_w 6.2. Figures S2 and S5 compare the observed and predicted geodetic measurements based on our inferred fault model (Figure 2). For InSAR fitting, there is generally good fit to both Sentinel-1 and ALOS-2 interferograms, except for some localized higher misfit along the assumed fault trace at the surface (Figure S5). These local misfits could be due to phase unwrapping errors or oversimplification of the fault geometry. In this study we assume a planar fault plane with constant dip angle, so our fault model is not able to describe very near field displacement related to shallower fault slip if the actual fault is listric or if the fault is curved along strike.

The inferred slip distribution indicates two distinct slip asperities at depth and is in agreement with preliminary study by *Piccardi et al.* [2016] and a seismic inversion study by *Tinti et al.* [2016]. Due to the smoothing effect of the elastic layers between the slip and the surface, we cannot be sure whether the slip between the asperities goes to zero or only a low value, but there must be a minimum in the slip to match the InSAR data. The total slip area (defined as slip greater than 40 cm) of the two asperities is ~70 km^2, and the peak slip of the north and south asperities is 1.3 and 1.0 m, respectively. The aftershocks in the first 2 weeks are located in the periphery of the two asperities (Figure 2a). Our inversion also shows up to ~40 cm fault slip

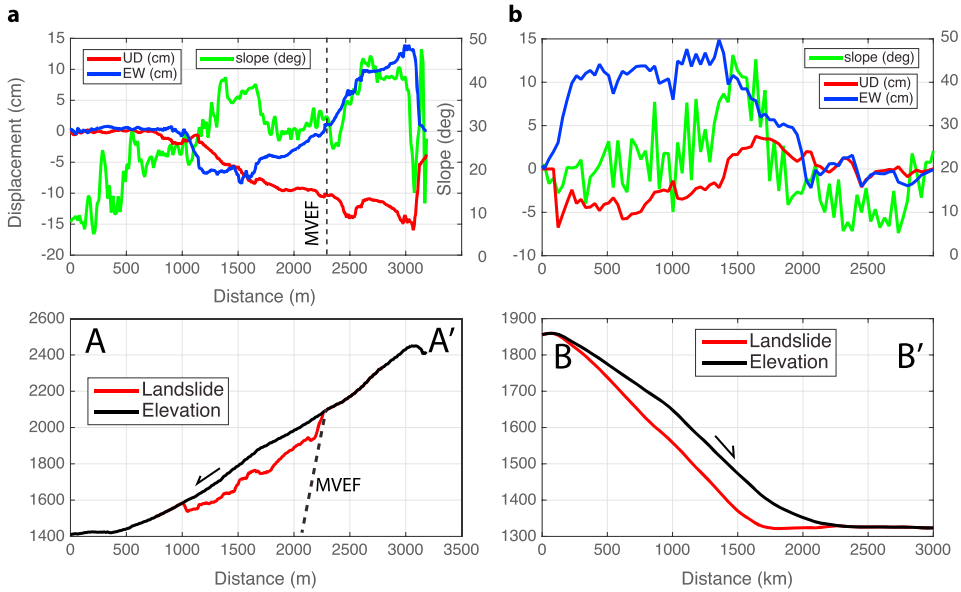

Figure 4. Cross sections (for locations, see Figure 3) of the triggered landslides at (a) Monte Vettore and (b) west of Castelluccio. In the upper panels, the green, blue, and red lines are the hillslope angle, east-west, and vertical displacements, respectively. In Figure 4a, the displacement components are derived from CSK descending and ALOS-2 ascending; in Figure 4b they are derived from ALOS-2 ascending and descending data. In the lower panels the red lines indicate the estimated base of the landslide and the black is topography from TanDEM-X IDEM.

at the shallowest (0–1 km) depth SW of Monte Vettore (Figures 1, 2a, and 2b). We will discuss whether this is actual fault slip or triggered landslides at Monte Vettore in section 5.

Recent studies by *Gruppo di Lavoro INGV sul Terremoto di Amatrice* [2016] and *Lavecchia et al.* [2016] proposed a two-fault model to explain the coseismic geodetic measurements. In their models, the two main asperities are on two separate fault segments north and south of the hypocenter. In supporting information Text S1, we test this alternative two-fault system and find similar fault parameters as found by *Gruppo di Lavoro INGV sul Terremoto di Amatrice* [2016] and *Lavecchia et al.* [2016]. However, the improvement of data fitting of this two-fault geometry is not significant (total chi-square misfit χ^2 reduces from 4.33 to 4.26), and we therefore consider the one-fault system as our preferred fault geometry.

5. Discussion and Conclusions

Our slip inversion shows no continuous slip between the main asperities at 3–6 km depth and the shallow (0–1 km depth) deformation near Monte Vettore with our preferred smoothing parameter. To understand stress transfer from deep to shallow depths, we use the two main slip asperities as the source of coseismic stress change and then calculate the static Coulomb stress change on the entire fault plane as well as the periphery of the region using Coulomb 3.3 [*Toda* et al., 2011], which uses boundary element calculations in a homogeneous elastic half-space. We calculate the Coulomb stress transfer model based on the inferred fault model parameters without taking shallow slip into account. Figure S6a shows a map view of Coulomb stress change at 1 km depth with receiver fault orientation as the main shock. A cross section view (Figure S6b) shows stress increase (i.e., promotes future fault failure) at shallower depth. Assuming receiver fault geometry as the inferred earthquake fault, the Coulomb stress transfer result shows more than 0.5 MPa Coulomb stress increase in the periphery of the two slip asperities and more than 1 MPa stress increase at the shallowest depth (Figure S6c). Despite this prediction of a large Coulomb stress change from the homogeneous elastic modeling, our InSAR analysis shows that the surface deformation near the MVEF is not normal fault slip but a deep-seated landslide. This could be due to the large differences in rheology between alluvial deposits and fractured rocks of the MVEF hanging wall and more competent rocks of the footwall.

According to our source slip distribution, the majority of the fault slip is north of the epicenter in the northern asperity, indicating substantial northward directivity. Part of the southern asperity is south of the epicenter,

so there was likely some southward directivity also in a bilateral rupture [*Tinti et al*., 2016]. Combination of the northward directivity and regional topography at the steep hillslopes in Monte Vettore and west of Castelluccio would suggest stronger ground shaking than was predicted from the USGS ShakeMap (http://earthquake.usgs.gov/earthquakes/eventpage/us10006g7d#map). However, the southward directivity for the southern asperity alone cannot explain the severe damage in Amatrice that is located south of the epicenter, despite equally strong ground motion (up to 0.5 g acceleration observed in Amatrice) [*NEIC*, 2016] predicted by USGS. The Amatrice town is built on an ~600 m wide ridge next to two active river channels, and the ridge is mostly made of Pleistocene alluvial deposits. As a result, a soft sedimentary ridge and local topographic focusing effects on the ground motion could be the cause of the stronger shaking in Amatrice.

To the north of the main coseismic deformation east and west of Castelluccio, we find at least two areas with localized surface deformation (red dashed squares in Figures 1a). Our inferred fault slip model (Figure 2) indicates that the shallower (0–1 km depth) slip can partly fit the localized deformation near Monte Vettore. However, with the high-resolution CSK descending interferogram, we find that these deformation areas may have different sources than fault slip due to a sharp termination of displacement at the bottom of the displacement (Figure 3a). With displacement related to the main fault slip removed (supporting information Text S2), the two localized deformation areas are NW and NE from where the maximum coseismic displacement separated from the fault slip asperities at depth. West of Monte Vettore (Figures 3a–3c), we find an area with much higher fringe density from the Monte Vettore foothills to the fault scarp of the Monte Vettore fault (MVEF) [*Galadini and Galli*, 2003]. The MVEF fault scarp runs along the western Monte Vettore foothills that is mostly made of Mesozoic limestone [*Bally et al*., 1986] and is considered active despite lack of historical earthquakes [*Galadini and Galli*, 2003]. On the other hand, there is no mapped active fault at another localized deformation west of Castelluccio (Figures 3d–3f).

For the deformation near Monte Vettore, the unwrapped phase indicates westward and/or downslope movement along the west facing side of the mountain, and the main deformation ranged ~1.8 km from the foothills to the MVEF fault scarp, corresponding to ~4.4 km^2 area. We find that this deformation extends no more than 5 km and is consistent with field survey after the earthquake [*Piccardi et al*., 2016]. In order to characterize the deformation along the hills, we use part of the Deutsches Zentrum für Luft- und Raumfahrt (DLR) 0.4 arc sec resolution intermediate digital elevation model (IDEM) from the TanDEM-X (TDX) satellite mission data collected in 2013. The TDX IDEM quality could vary locally due to layover or foreshortening. Hillslope angles were measured by taking a finite-difference scheme using equation (S9) from the DEM [*Perron et al*., 2008]. For the landslide near Monte Vettore, we use the CSK descending and ALOS-2 ascending interferograms (Figures 4b and 4c) to estimate east-west and vertical displacements assuming no north-south motion using equation (S7) in supporting information Text S2 (Figure 4a). We do not include Sentinel-1 interferograms in the landslide analysis because there is more phase unwrapping errors near Monte Vettore than ALOS-2 or CSK interferograms. We compare a SW-NE cross section of this displacement, and we find that the east-west displacement is anticorrelated to the hillslope (the blue and green lines between distance 1000 and 2300 m in Figure 4a). For the deformation west of Castelluccio, we used the ALOS-2 descending and ascending interferograms to estimate the east-west and vertical displacements along the east facing side of the hill (Figure 4b). Similar to the displacement transect near Monte Vettore, the vertical displacement transect correlates with the hillslope (the red and green lines between 500 and 2000 m in Figure 4b, respectively). These localized deformations imply a relatively shallow source of slip. The width (along NE-SW) of this landslide is ~1.9 km, and the area is ~2.5 km^2.

Booth et al. [2013] suggest a simple inversion scheme to estimate the depth distribution along a deep-seated landslide in La Clapière, France. This method is based on the conservation of mass with constant material density during landslides and the use of repeat stereo imagery and DEM. *Delbridge et al*. [2016] apply similar methodology to the Slumgullion landslide in Colorado, USA. Here we estimate surface-parallel horizontal and vertical displacements based on ascending and descending interferograms and TDX IDEM (supporting information Text S2). For the landslide west of Castelluccio, both ascending and descending ALOS-2 interferograms show good coherence at the landslide area (Figures 3e and 3f). Based on our analysis described in supporting information Text S1, we find that the base of the slide is generally between 100 and 80 m for landslides near Monte Vettore and west of Castelluccio, depending on the rheology of the landslides [*Booth et al*., 2013] (Figures 4 and S7). This result suggests a much shallower source of slip than any possible triggered

shallow slip along MVEF. More importantly, if a M_w 6 event has been repeatedly occurring in history, triggered deep-seated landslide that terminates at this preexisting fault scarp could have significantly influenced the long-term fault slip rate estimate using paleoseismology [e.g., *Galadini and Galli*, 2003].

In this study, we investigate the fault geometry and the slip distribution of the 2016 M_w 6.2 Amatrice earthquake based on geodetic data sets including 105 GPS measurements and four ascending or descending interferograms. The inferred fault geometry is in good agreement with seismic inversions such as NEIC and GCMT solutions. With relatively short temporal and spatial baseline between SAR acquisitions, InSAR can reveal details of the near-to-far-field coseismic displacement, which is important in constraining source slip distribution as well as assessing surface damage in a short period of time. Our work demonstrates natural hazard response in characterizing surface deformation as well as source slip distribution in a median size continental earthquake at shallow depth. New satellites are now revealing InSAR-based surface deformation within a week after natural hazard events. We hope that in the near future, quick hazard responses will be more publically accessible and provide information to responding agencies.

Acknowledgments

We thank an anonymous reviewer for giving insightful comments that improved the original manuscript. The Sentinel-1 images contain modified Copernicus data. Original ALOS-2 data are copyright by Japan Aerospace Exploration Agency (JAXA) and were provided under JAXA ALOS RA-4 projects (S.H. Yun) and P1372 (E. Fielding). COSMO-SkyMed products were processed by JPL under license from ASI; Original COSMO-SkyMed Products-©ASI-Agenzia Spaziale Italiana-(2016). TanDEM-X IDEM data were provided by Deutsches Zentrum für Luft- und Raumfahrt (DLR) under proposal IDEM_CALVAL0052. The geologic map of Lazio Region is from www.dati.lazio.it (last data accessed 7 September 2016), and the geologic map of Marche region is from www.ambiente.marche.it (last data accessed 7 September 2016). Aftershocks relocation data are from the ISIDE INGV database. The Sentinel ascending interferogram was processed by the JPL Advanced Rapid Imaging and Analysis (ARIA) Center. We thank INGV for making the GPS measurements publicly available. The interferograms and the fault model are available upon request to the corresponding author. Part of this research was supported by the NASA Earth Surface and Interior focus area and performed at the Jet Propulsion Laboratory, California Institute of Technology. M.-H. Huang, C. Liang, and P. Milillo are supported by appointments to the NASA Postdoctoral Program at the Jet Propulsion Laboratory, administered by the Universities Space and Research Association through a contract with NASA.

References

Atzori, S., I. Hunstad, M. Chini, S. Salvi, C. Tolomei, C. Bignami, S. Stramondo, E. Trasatti, A. Antonioli, and E. Boschi (2009), Finite fault inversion of DInSAR coseismic displacement of the 2009 L'Aquila earthquake (central Italy), *Geophys. Res. Lett.*, *36*, L15305, doi:10.1029/2009GL039293.

Bally, A. W., L. Burbi, C. Cooper, and R. Ghelardoni (1986), Balanced sections and seismic reflection profiles across the central Apennines, *Mem. Soc. Geol. Ital.*, *35*, 257–310.

Bekaert, D. P. S., A. Hooper, and T. J. Wright (2015a), Reassessing the 2006 Guerrero slow-slip event, Mexico: Implications for large earthquakes in the Guerrero Gap, *J. Geophys. Res. Solid Earth*, *120*, 1357–1375, doi:10.1002/2014jb011557.

Bekaert, D. P. S., A. Hooper, and T. J. Wright (2015b), A spatially variable power law tropospheric correction technique for InSAR data, *J. Geophys. Res. Solid Earth*, *120*, 1345–1356, doi:10.1002/2014JB011558.

Blumetti, A. M., F. Dramis, and A. M. Michetti (1993), Fault generated mountain fronts in the central Apennines (Central Italy): Geomorphological features and seismotectonic implications, *Earth Surf. Processes Landforms*, *18*, 203–223.

Boncio, P., G. Lavecchia, G. Milana, and B. Rozzi (2004), Seismogenesis in Central Apennines, Italy: An integrated analysis of minor earthquake sequences and structural data in the Amatrice-Campotostop area, *Ann. Geophys.*, *47*, 1723–1742.

Booth, A. M., M. P. Lamb, J.-P. Avouac, and C. Delacourt (2013), Landslide velocity, thickness, and rheology from remote sensing: La Clapière landslide, France, *Geophys. Res. Lett.*, *40*, 4299–4304, doi:10.1002/grl.50828.

Cheloni, D., et al. (2014), Coseismic and post-seismic slip of the 2009 L'Aquila (central Italy) M_w 6.3 earthquake and implications for seismic potential along the Campotosto fault from joint inversion of high-precision levelling, InSAR and GPS data, *Tectonophysics*, doi:10.1016/j.tecto.2014.03.009.

Chen, C., and H. Zebker (2002), Phase unwrapping for large SAR interferograms: Statistical segmentation and generalized network models, *IEEE Trans. Geosci. Rem. Sens.*, *40*, 1709–1719, doi:10.1109/tgrs.2002.802453.

Cimellaro, G. P. (2016), Field reconnaissance on August 25th, after August 24th, 2016 Central Italy earthquake. [Available at http://peer.berkeley.edu/pdf/160829_Central%20Italy_earthquake.pdf.]

Cirella, A., A. Piatanesi, E. Tinti, M. Chini, and M. Cocco (2012), Complexity of the rupture process during the 2009 L'Aquila, Italy, earthquake, *Geophys. J. Int.*, *190*, 607–621, doi:10.1111/j.1365.246X.2012.05505.x.

D'Agostino, N. (2014), Complete seismic release of tectonic strain and earthquake recurrence in the Apennines (Italy), *Geophys. Res. Lett.*, *41*, 1155–1162, doi:10.1002/2014GL059230.

D'Agostino, N., A. Avallone, D. Cheloni, E. D'Anastasio, S. Mantenuto, and G. Selvaggi (2008), Active tectonics of the Adriatic region from GPS and earthquake slip vectors, *J. Geophys. Res.*, *113*, B12413, doi:10.1029/2008JB05860.

Delbridge, B. G., R. Bürgmann, E. Fielding, S. Hensley, and W. H. Schulz (2016), Three-dimensional surface deformation derived from airborne Interferometric UAVSAR: Application to the Slumgullion Landslide, *J. Geophys. Res. Solid Earth*, *121*, 3951–3977, doi:10.1002/2015JB012559.

Dziewonski, A. M., T.-A. Chou, and J. H. Woodhouse (1981), Determination of earthquake source parameters from waveform data for studies of global and regional seismicity, *J. Geophys. Res.*, *86*, 2825–2852, doi:10.1029/JB086iB04p02825.

Farr, T. G., et al. (2007), The Shuttle Radar Topography Mission, *Rev. Geophys.*, *45*, RG2004, doi:10.1029/2005RG000183.

Fialko, Y., M. Simons, and D. Agnew (2001), The complete (3D) surface displacement field in the epicentral area of the 1999 M_w 7.1 Hector Mine earthquake, southern California, from space geodetic observations, *Geophys. Res. Lett.*, *28*, 3063–3066, doi:10.1029/2001GL013174.

Galadini, F., and P. Galli (2003), Paleoseismology of silent faults in the Central Apennines (Italy): The Mt. Vettore and Laga Mts. faults, *Ann. Geophys.*, *46*, 815–836.

Galli, P., R. Camassi, R. Azzaro, F. Bernardini, S. Castenetto, D. Molin, E. Peronace, A. Rossi, M. Vecchi, and A. Tertulliani (2009), Terremoto de L'Aquila del 6 Aprile 2009: Rilievo macrosismico, distribuzione delle intensità macrosismiche ed implicazioni sismotettoniche, *Il Quaternario*, *22*, 235–246.

Gruppo di Lavoro INGV sul Terremoto di Amatrice (2016), Secondo rapporto di sintesi sul Terremoto di Amatrice ML 6.0 del 24 Agosto 2016 (Italia Centrale), doi:10.5281/zenodo.154400.

Huang, M.-H., D. Dreger, R. Bürgmann, S.-H. Yoo, and M. Hashimoto (2013), Joint inversion of seismic and geodetic data for the source of the 2010 March 4, M_w 6.3 Jia-Shian, SW Taiwan, earthquake, *Geophys. J. Int.*, *193*, 1608–1626, doi:10.1093/gji/ggt058.

INGV Working Group "GPS Geodesy (GPS data and data analysis center)" (2016), Preliminary co-seismic displacements for the August 24, 2016 ML 6, Amatrice (central Italy) earthquake from the analysis of continuous GPS stations, doi:10.5281/zenodo.61355.

Kaverina, A., D. Dreger, and E. Price (2002), The combined inversion of seismic and geodetic data for the source process of the 16 October 1999 M_w 7.1 Hector Mine, California, earthquake, *Bull. Seism. Soc. Am.*, *92*, 1266–1280, doi:10.1785/0120000907.

Lavecchia, G., et al. (2016), Ground deformation and source geometry of the August 24, 2016 Amatrice earthquake (Central Italy) investigated through analytical and numerical modeling of DInSAR measurements and structural-geological data, *Geophys. Res. Lett.*, *43*, 12,389–12,398, doi:10.1002/2016GL071723.

Lundgren, P., and S. Stramondo (2002), Slip distribution of the 1997 Umbria-Marche earthquake sequence: Joint inversion of GPS and synthetic aperture radar interferometry data, *J. Geophys. Res. 107*(B11), 2316, doi:10.1029/2000JB000103.

Margheriti, S. M., F. Mele, G. Selvaggi, A. Basili, and E. Boschi (1998), The 1997 Umbria-Marche, Italy, earthquake sequence, *Geophys. Res. Lett.*, *25*, 2861–2864, doi:10.1029/98GL51842.

Monachesi, G., and V. Castelli (eds.) (1992), Sismicità dell'area aquilano-teramana dalla "analisi attraverso i cataloghi", Rapporto tecnico per la Regione Abruzzo, *Osservatorio Geofisico Sperimentale, Macerata*, 245 pp.

National Earthquake Information Center (NEIC) (2016), *M6.2*-Italy (United States Geological Survey, 2016). [Available at http://earthquake.usgs.gov/earthquakes/eventpage/us10006g7d#scientific.]

Perron, J. T., W. E. Dietrich, and J. W. Kirchner (2008), Controls on the spacing of first-order valleys, *J. Geophys. Res.*, *113*, F04016, doi:10.1029/2007JF000977.

Piccardi, L., et al. (2016), The August 24, 2016, Amatrice earthquake (M_w 6.0): Field evidence of on-fault effects-Preliminary report, 31 pp. [Available at http://www.isprambiente.gov.it/files/notizie-ispra/notizie-2016/sisma-italia-centrale/REPORT_Amatrice_en_2016_09_16.compressed.pdf.]

Postpischl, D. (Ed.) (1985), Catalogo dei terremoti Italiani dall'anno 1000 al 1980. Quaderni della ricerca scientifica, 114 2B, Bologna.

Rosen, P. A., E. Gurrola, G. F. Sacco, and H. Zebker (2012), The InSAR scientific computing environment, Proc. EUSAR, Nuremberg, Germany, 730–733.

Rovida A., M. Locati, R. Camassi, B. Lolli, and P. Gasperini (Eds.) (2016), CPTI15, the 2015 version of the Parametric Catalogue of Italian Earthquakes. *Istituto Nazionale di Geofisica e Vulcanologia*, doi:10.6092/INGV.IT-CPTI15.

Stramondo, S., et al. (1999), The September 26, 1997 Colfiorito, Italy, earthquakes: Modeled coseismic surface displacement from SAR interferometry and GPS, *Geophys. Res. Lett.*, *26*, 883–886, doi:10.1029/1999GL900141.

Sudhaus, H., and S. Jónsson (2009), Improved source modelling through combined use of InSAR and GPS under consideration of correlated data errors: application to the June 2000 Kleifarvatn earthquake, Iceland, *Geophys. J. Int.*, *176*, 389–404, doi:10.1111/j.1365-246x.2008.03989.x.

Tinti, E., L. Scognamiglio, A. Michelini, and M. Cocco (2016), Slip heterogeneity and directivity of the ML 6.0, Amatrice earthquake estimated with rapid finite-fault inversion, *Geophys. Res. Lett.*, *43*, 10,745–10,752, doi:10.1002/2016GL071263.

Toda, S., R. S. Stein, V. Sevilgen, and J. Lin (2011), Coulomb 3.3 Graphic-rich deformation and stress-change software for earthquake, tectonic, and volcano research and teaching—User guide: U.S. Geol. Surv. Open File Rep., vol. *63*, pp. 2011–1060. [Available at http://pubs.usgs.gov/of/2011/1060/.]

Wang, R., F. Lorenzo Martin, and F. Roth (2003), Computation of deformation induced by earthquakes in a multi-layered elastic crust—FORTRAN programs EDGRN/EDCMP, *Comput. Geosci.*, *29*, 195–207.